Journal of Power Sources 483 (2021) 229148

Contents lists available at ScienceDirect

Journal of Power Sources

journal homepage: www.elsevier.com/locate/jpowsour

Mapping the architecture of single lithium ion electrode particles in 3D, using electron backscatter diffraction and machine learning segmentation

Orkun Furat [a,*], Donal P. Finegan [b,*], David Diercks [c], Francois Usseglio-Viretta [b], Kandler Smith [b], Volker Schmidt [a]

[a] Institute of Stochastics, Ulm University, 89069 Ulm, Germany
[b] National Renewable Energy Laboratory, 15013 Denver W Parkway, Golden, CO 80401, USA
[c] Colorado School of Mines, 1500 Illinois St, Golden, CO 80401, USA

ARTICLE INFO

Keywords:
Convolutional neural network
Statistical image analysis
Model fitting
Copula
Lithium ion battery
Electron backscatter diffraction

ABSTRACT

Accurately quantifying the architecture of lithium ion electrode particles in 3D is critical to understanding sub-particle lithium transport, rate limitations, and degradation mechanisms within lithium ion batteries. Most commercial positive electrode materials consist of polycrystalline particles, where intra-particle grains have a range of morphologies and orientations. Here, focused ion beam slicing in sequence with electron backscatter diffraction is used to accurately quantify intra-particle grain morphologies in 3D. The intra-particle grains are identified using convolution neural network segmentation and distinctly labeled. Efficient morphological characterization of the grain architectures is achieved. Bivariate probability density maps are developed to show correlative relationships between morphological grain descriptors. The implication of morphological features on cell performance, as well as the extension of this dataset to guide artificial generation of realistic particle architectures for 3D multi-physics models, is discussed.

1. Introduction

The demand for high-performance lithium (Li) ion batteries is greater now than ever before. Within electric vehicles, Li-ion batteries are expected to provide the user with more than 300 miles of range on a single charge, to charge quickly when needed, and to have a life-time commensurate with thousands of charge and discharge cycles. To achieve these performance metrics, in-depth understanding and control of Li transport and degradation mechanisms within the electrodes is needed. Layered Li-ion positive electrode materials such as $LiNi_xMn_yCo_zO_2$ (NMC) are common in commercial Li-ion batteries used for electric vehicles. NMC particles are often polycrystalline with intra-particle grains that guide the intercalating Li along 2D planes with the crystal structure of NMC [1]. When the grains lithiate they expand anisotropically in the direction of the crystal structure, which can lead to intergranular stresses and cause the particles to crack [2,3]. This strain-induced cracking is considered to be one of the major causes of capacity fade within Li-ion cells, primarily from increasing the exposed surface area to react with electrolyte and form interphase layers, as well as degrading the connectivity between grains [4]. It has been shown that electrodes with less cracking have better lifetimes [5], thus ideally particle architectures that minimize strain without sacrificing performance should be synthesized.

In-depth operando or multiphysics models are needed to understand the spatial and temporal evolution of inter-particle strains and the formation of cracks. Yet, despite the importance of understanding the grain properties of particles, experimental tools to characterize electrode particle architectures are not widely available or practiced. Some non-destructive X-ray techniques have recently shed light into the influence of grain architectures on particle degradation, but studies are still limited. Liu et al. [4] demonstrated a combination of X-ray diffraction with transmission X-ray microscopy (TXM) to follow the activity of particles and visualize sub-particle cracks, and Xue et al. [1] also used TXM to follow local valence states of Ni in NMC creating a map of charge distribution. However, TXM cannot capture the grain orientations and thus is limited in its ability to create a link between grain properties and the propensity of particles to degrade. X-ray diffraction computed tomography (XRDCT) may hold promise for mapping the distinct grain orientations and responses during operation [6], but its resolution is currently limited to around 1 μm and access to this technique is constrained due to it only being available at a small number of synchrotron facilities.

EBSD can be applied to spatially resolve grain orientations from smooth cross-sections of materials [7] and the image quality (IQ) maps

* Corresponding authors.
E-mail addresses: orkun.furat@uni-ulm.de (O. Furat), donal.finegan@nrel.gov (D.P. Finegan).

https://doi.org/10.1016/j.jpowsour.2020.229148
Received 4 August 2020; Received in revised form 19 September 2020; Accepted 28 October 2020
Available online 16 November 2020

from the imaging are a useful means to visualize the grain architectures through changes in the contrast at grain boundaries [8,9]. EBSD systems are typically incorporated into lab-based scanning electron microscope (SEM) instruments and are thus widely accessible to many research laboratories. Sequential EBSD imaging followed by focused ion beam (FIB) milling of the analyzed sample produces a sequence of EBSD images, i.e., a tomographic image dataset of the sample [10]. The output images of EBSD can be segmented and distinct grains identified. More precisely, using advanced image processing techniques it is possible to compute descriptors of the material's microstructure. For materials which are composed of two or more phases, descriptors like the porosity, tortuosity and constrictivity can efficiently characterize the microstructure [11]. When the material is composed of grains or particles it is possible to compute size and shape characteristics of each individual grain/particle which allows the fitting of parametric probability distributions to the histograms of the considered characteristics [12–14]. For correlated grain or particle characteristics so-called copulas can be used to fit multivariate probability distributions which are much more informative than marginal distributions [13]. Parametric models of uni- and multivariate probability distributions provide an efficient way for describing a material's microstructure which, for example, allows for an easy quantitative comparison of different materials [15]. Furthermore, probability distributions of microstructure characteristics can be used to fit parametric stochastic models for the entire 3D microstructure which can generate virtual microstructures. For example, models based on mathematical tessellation models can generate random grain architectures [16,17]. From these microstructure models a broad spectrum of virtual but realistic grain architectures can be drawn which can be used in numerical simulations for investigating the influence of the microstructure's geometry on macroscopic physical properties [18–24].

In the present paper, we investigate the inner 3D grain architecture of NMC particles by stochastically modeling the distribution of grain characteristics using FIB-EBSD image data. Therefore, in a first step, we compute a grain-wise segmentation of image data using a combination of techniques from machine learning [25] and "conventional" image processing [26]. Note that there are segmentation approaches for image data of polycrystalline materials which rely solely on "conventional" image processing methods. They often require many preprocessing steps, followed by a marker-based watershed segmentation with additional postprocessing steps [27,28]. Moreover, these approaches often require careful and tedious calibration of image processing parameters. Therefore, in the present paper, we deploy a convolutional neural network, namely a 3D U-net [29,30], for enhancing grain boundaries depicted in the FIB-EBSD data. This reduces the amount of preprocessing needed prior to the application of the segmentation algorithm. For training the network, we modify the loss function such that training can be performed with just a few labeled slices of the 3D FIB-EBSD data [31]. This approach has the advantage of not requiring volumetric labeled data which can be tedious to obtain, e.g., by manual labeling. After training, we apply the network to the entire 3D image data, resulting in a new 3D image with enhanced grain boundaries. Then, individual grains are extracted from the latter by using a marker-based watershed algorithm [28,32]. From the segmented image data, we extract individual grains and compute characteristics describing their size and shape like, for example, their volume-equivalent diameter and sphericity. For each considered grain characteristic, we fit parametric probability distributions (e.g., log-normal, gamma, Weibull distribution) to their histograms using maximum likelihood estimation [33]. In this manner the univariate distribution of each individual grain characteristic is efficiently described by just a few parameters. Since grain characteristics are, in general, correlated we also model joint distributions of pairs of grain characteristics. More precisely, we use parametric copulas [34] for describing the bivariate probability distributions of pairs of grain characteristics, leading to a more informative description of the NMC particle's grain characteristics than univariate distributions can provide. In a forthcoming paper, these models for characteristics of individual grains will be used to construct parametric stochastic models for the holistic inner 3D grain architecture of NMC particles, based on random tessellations.

2. Materials & methods

2.1. Sample details and preparation

A calendared positive electrode was used, which consisted of TODA $LiNi_{0.5}Mn_{0.2}Co_{0.2}O_2$ (NMC532) particles in a 70 µm thick electrode coating of 90 wt% NMC532, 5 wt% C45 Timcal conductive carbon, and 5 wt% PVdF binder, on a 20 µm thick aluminum current collector. N-Methyl-2-pyrrolidone (NMP) solvent was applied on the electrode to dissolve the binder, wiped from the electrode using a rubber spatula, smeared onto a fresh copper sheet, and allowed to dry. The smeared electrode material facilitated identification of single particles connected directly to the copper film in the SEM system, and thus created an ideal condition for isolating particles that have excellent electrical connection for FIB–EBSD. A small tab of the smeared copper sheet was cut and applied to an SEM stub with conductive carbon adhesive.

2.2. Imaging of NMC particles using FIB-EBSD

SEM and EBSD images were acquired with an FEI Helios NanoLab 600i equipped with an EDAX-EBSD detector. A 30 kV 2.5 nA Ga focused ion beam was used to mill away 50 nm sections of material between each EBSD scan. The EBSD scans were performed with 50 nm step sizes in x- and y-direction in a square array. EBSD data were processed with OIM Analysis v8 (EDAX, USA). Diffraction patterns were fit to a trigonal crystal system (space group R-3m) with $a = b = 2.87$ Å, and $c = 14.26$ Å to obtain the orientation of the crystal at each pixel (a, b, and c are the edge lengths of the hexagonal unit cell which contains the trigonal structure). The software produced text files containing spatially resolved confidence index, image quality, and Bunge-Euler angle data.

2.3. Processing of image data

In order to characterize the 3D grain microstructure of NMC particles from FIB-EBSD image data, the latter has to be segmented. More precisely, we have to identify grains depicted in image data. This allows the extraction of individual grains such that it becomes possible to compute their size and shape characteristics like, for example, their volume-equivalent diameter and sphericity. For that purpose, we utilize the IQ-channel of the EBSD image stack. The segmentation is achieved in three steps. First, we align the stack of EBSD image data. Then, the grain boundaries in the aligned 3D image are enhanced using a convolutional neural network [30]. Finally, the segmentation is completed by applying a marker-based watershed algorithm [28,32].

2.3.1. Stack alignment

Since the stack of EBSD images was acquired by milling the NMC particle under consideration using a focused ion beam followed by 2D EBSD imaging, the stack of images can be misaligned, see Fig. 1a. Therefore, in a first step, we use the IQ-channel of the EBSD data to align the image stack, applying the pyStackReg package in Python [35]. The resulting aligned image stack is visualized in Fig. 1b. From here on, we denote the aligned 3D image by the map $I : W \to \mathbb{R}$ where $W = \{1, \dots, 235\} \times \{1, \dots, 221\} \times \{1, \dots, 91\} \subset \mathbb{Z}^3$ is the discretized sampling window, i.e., $I(x)$ denotes the image's value at $x \in W$. We also say that the image I has a resolution of $235 \times 221 \times 91$ voxels.

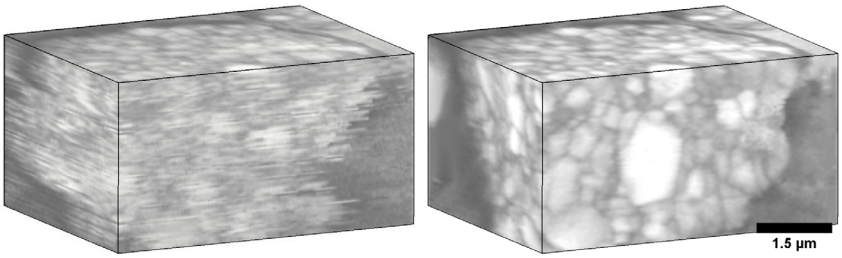

(a) (b)

Fig. 1. Volumetric cutout of the EBSD data prior to (a) and after stack alignment (b).

2.3.2. CNN-based grain boundary enhancement

In the next image processing step, similar to the method used in [30], we enhance the grain boundaries of the 3D image I using a CNN, namely a 3D U-net architecture, see [29]. More precisely, we want to determine a CNN, denoted by D, which can predict, from the aligned EBSD data I, three images $G_\mathrm{b}, G_\mathrm{i}, B$ corresponding to grain boundaries, grain interiors and the background of I, respectively. The grain boundary image G_b of I is given by

$$G_\mathrm{b}(x) = \begin{cases} 1, & \text{if } x \text{ corresponds to a grain boundary,} \\ 0, & \text{else,} \end{cases} \tag{1}$$

for each $x \in W$. Analogously, the grain interior image G_i and the background image B are defined, see Fig. 2. Using this notation the CNN D has to be able to predict $G_\mathrm{b}, G_\mathrm{i}, B$ from I, i.e., we consider the regression problem $D(I) \approx (G_\mathrm{b}, G_\mathrm{i}, B)$. Moreover, this predictive property of D should hold for each cutout of I and the corresponding cutouts of the images $G_\mathrm{b}, G_\mathrm{i}, B$. Now we describe how a CNN can be determined (i.e. trained) which can make these predictions reliably.

First, we choose a suitable parametric family of functions $\{D_\xi : \xi \in \Xi\}$ from which D has to be determined, where Ξ denotes the space of parameters. In our scenario we use as the parametric family the set of 3D U-nets [30,31] with three output channels and the Softmax function [25] as the activation function of the output layer, see Fig. 3. Consequently, for any 3D input image the output of a U-net D_ξ with parameter ξ (i.e., the network's weights) are three images $\hat{Y}_1, \hat{Y}_2, \hat{Y}_3$. The Softmax function ensures that the voxel values of the output images are normalized and represent probabilities, i.e., we have $0 \leq \hat{Y}_1(x), \hat{Y}_2(x), \hat{Y}_3(x) \leq 1$ and $\hat{Y}_1(x) + \hat{Y}_2(x) + \hat{Y}_3(x) = 1$ for each voxel $x \in W$. Therefore, the chosen parametric family of functions is able to reassemble the target images $G_\mathrm{b}(x), G_\mathrm{i}(x), B(x)$ which also fulfill the equation

$$G_\mathrm{b}(x) + G_\mathrm{i}(x) + B(x) = 1 \tag{2}$$

for each voxel $x \in W$ since it either belongs to the grain boundary, grain interior or the background.

In order to measure how well a CNN with parameter ξ performs in the task of predicting the grain boundaries, grain interiors and the background from EBSD data, we use a loss function, namely the categorical cross entropy ℓ given by

$$\ell\left((\hat{Y}_k)_{k=1,2,3}, (Y_k)_{k=1,2,3}\right) = -\sum_{x \in W'} \sum_{k=1}^{3} \hat{Y}_k(x) \log Y_k(x), \tag{3}$$

where Y_1, Y_2, Y_3 denote cutouts from $G_\mathrm{b}, G_\mathrm{i}, B$ in a cuboidal sampling window $W' \subset W$. The predictions $(\hat{Y}_k)_{k=1,2,3}$ in Eq. (3) are given by

$$(\hat{Y}_k)_{k=1,2,3} = D_\xi(J), \tag{4}$$

where J is a cutout of the aligned EBSD IQ image I taken from the same sampling window W'. Then, an optimal parameter constellation ξ for which the CNN makes reliable predictions is obtained by minimizing the values of the loss function ℓ given in Eq. (3) for randomly chosen cutout windows W'. The minimization of the loss function which, in this context, is referred to as training of the CNN is often performed using a stochastic gradient descent algorithm [25,36].

However, in order to train a CNN we require labeled data, i.e., the images $G_\mathrm{b}, G_\mathrm{i}, B$ depicting the grain boundaries, grain interiors and the background, respectively. Sometimes, in the field of materials science, labeled data can be obtained by performing a different (more expensive) measurement of the same specimen, see [12,13,30]. As an alternative, it is possible to manually label the image data. However, this can be tedious, especially when one has to label large 3D datasets. Therefore, in our scenario, we train the CNN with sparsely labeled data [31]. More precisely, we manually label the data I solely in four slices located at the coordinates $x = (x_1, x_2, x_3) \in W$ with $x_3 \in \{26, 37, 49, 60\}$. Thus, instead of having the full 3D grain boundary information of G_b we have a sparsely labeled grain boundary image $\widetilde{G}_\mathrm{b}$ given by

$$\widetilde{G}_\mathrm{b}(x) = \begin{cases} 1, & \text{if } x_3 \in \{26, 37, 49, 60\} \text{ and } x \\ & \text{corresponds to a grain boundary,} \\ 0, & \text{else,} \end{cases} \tag{5}$$

for each $x = (x_1, x_2, x_3) \in W$. The sparsely labeled images $\widetilde{G}_\mathrm{i}$ and $\widetilde{B}$ are defined analogously. Furthermore, when working with sparsely labeled data, we have to restrict the loss function's evaluation of the discrepancy between predictions $(\hat{Y}_k)_{k=1,2,3}$ and target images $(Y_k)_{k=1,2,3}$ to labeled voxels $x \in W$ with $x_3 \in \{26, 27, 49, 60\}$. Therefore, in the context of the present paper, we use the modified loss function $\widetilde{\ell}$ given by

$$\widetilde{\ell}\left((\hat{Y}_k)_{k=1,2,3}, (Y_k)_{k=1,2,3}\right) = -\frac{1}{\sum_{x \in W'} M(x)} \sum_{x \in W'} \sum_{k=1}^{3} M(x) \hat{Y}_k(x) \log Y_k(x), \tag{6}$$

where Y_1, Y_2, Y_3 denote cutouts from $\widetilde{G}_\mathrm{b}, \widetilde{G}_\mathrm{i}, \widetilde{B}$ in a cuboidal sampling window $W' \subset W$ and the mask of labeled voxels $M : W \to \{0, 1\}$ is given by

$$M(x_1, x_2, x_3) = \begin{cases} 1, & \text{if } x_3 \in \{26, 37, 49, 60\}, \\ 0, & \text{else.} \end{cases} \tag{7}$$

Using this modified loss-function, we trained the U-net, using the Adam algorithm with a batchsize of 1 [36]. Hereby, the batches consisted of cutouts J taken from the aligned EBSD image I with a size of $80 \times 80 \times 80$ voxels and cutouts $(Y_k)_{k=1,2,3}$ taken from the sparsely labeled images at the same position as cutout J. In order to increase the amount of training data and the robustness of the trained network we used data augmentation by isometrically transforming the training data. More precisely, we randomly rotated the images $I, \widetilde{G}_\mathrm{b}, \widetilde{G}_\mathrm{i}, \widetilde{B}, M$ in the same manner prior to taking random cutouts as described above.

After the training procedure, the trained network, denoted by D, was applied on the entire 3D image stack I. The results $(\hat{G}_\mathrm{b}, \hat{G}_\mathrm{i}, \hat{B}) = D(I)$ are visualized in Figs. 2e and 2f for a planar 2D section for which labeled images $(G_\mathrm{b}, G_\mathrm{i}, B)$ were available for training. For the purpose of visual validation Fig. 4 shows the network's prediction for a non labeled slice.

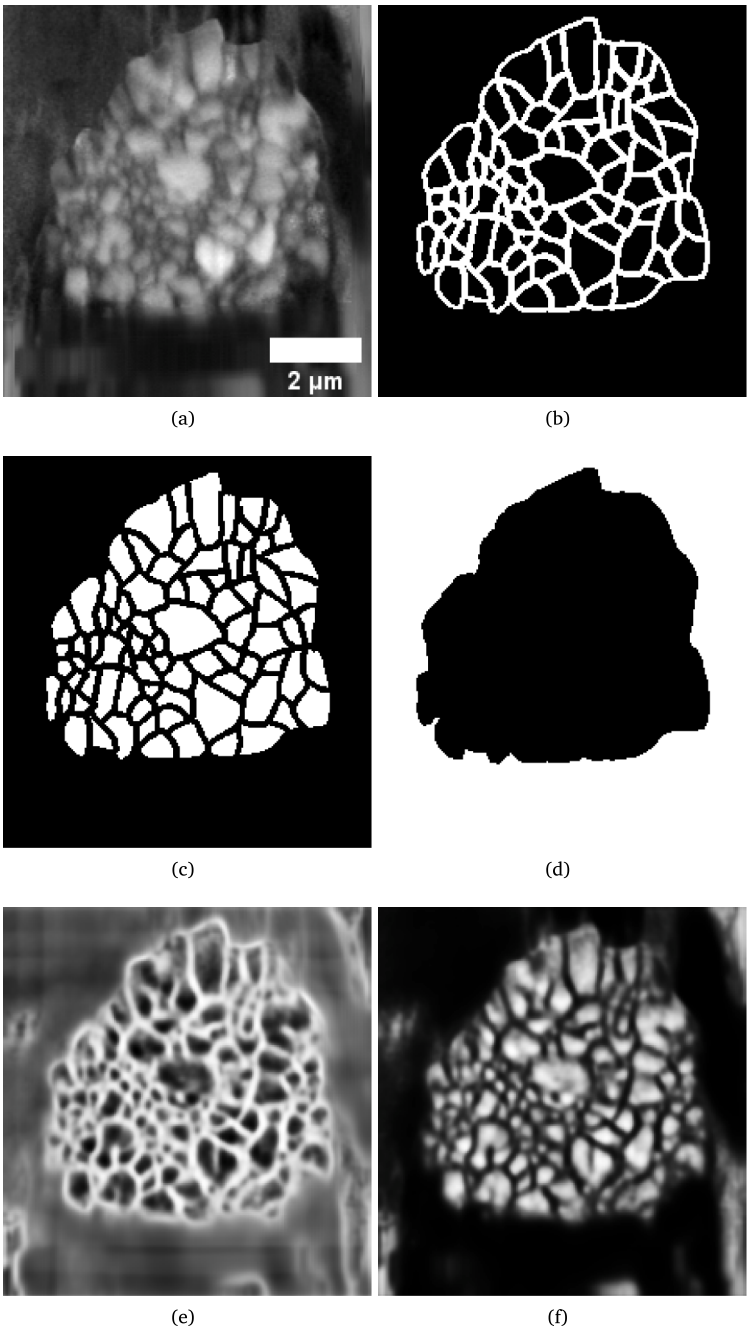

Fig. 2. Cross section through the EBSD IQ image I (a), the image G_b depicting grain boundaries (b), the grain interior image G_i (c) and the background image B (d). The corresponding predictions $\widehat{G}_b$ (e), $\widehat{G}_i$ (f) for the grain boundaries and the grain interior, respectively, of the trained CNN.

2.3.3. *Watershed-based segmentation of the image data*

The trained network's predictions $\widehat{G}_b, \widehat{G}_i, \widehat{B}$ of the grain boundaries, the grain interiors and the background do not yet provide a segmentation of the image data into individual grains. More precisely, the value $\widehat{G}_b(x)$ can be interpreted as the probability of $x \in W$ corresponding to the grain boundary network. Due to the "fuzzy" nature of these predictions the latter have to be further processed. Therefore, we utilize the so-called watershed algorithm to segment the grain boundary predictions $\widehat{G}_b$ into individual grains [32]. Starting from each local minimum in $\widehat{G}_b$, the watershed algorithm performs region growths, segmenting $\widehat{G}_b$ into multiple regions. In the grain boundary predictions the local minima tend to be located in grain interiors. However, since the watershed algorithm assigns to each local minimum its own region, noise or small local fluctuations in $\widehat{G}_b$ can introduce multiple local minima in a single grain's interior which leads to the watershed algorithm wrongly segmenting such a grain into multiple regions. Therefore, prior to the application of the watershed algorithm, we compute the h-minima transform of $\widehat{G}_b$ which is able to suppress such unnecessary local minima [32]. A planar 2D section through the resulting segmentation is depicted in Fig. 5a, where we can see that some regions of this segmentation belong to the background. Therefore, we remove the background in this initial segmentation by setting the labels of voxels $x \in W$ to 0 if these voxels belong to the background with a large probability, i.e., if $\widehat{B}(x) > h$ with some manually chosen threshold $0 < h < 1$, see Fig. 5b. Since this processing step does not remove all regions outside of the NMC particle entirely, we then manually remove the few remaining "background regions", see Fig. 5c.

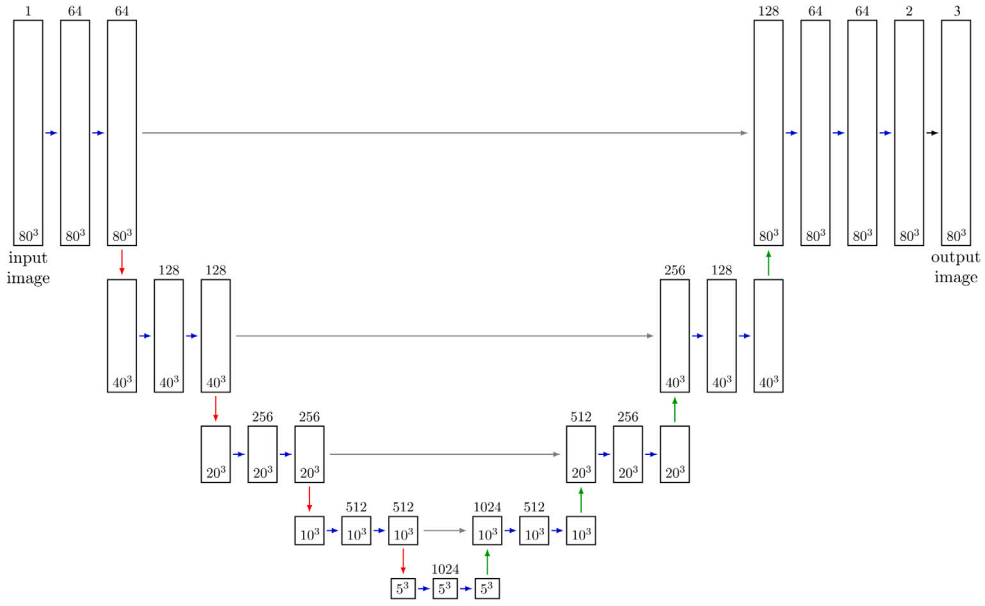

Fig. 3. Architecture of the 3D U-net considered in the present paper. The scheme is licensed under the creative commons attribution 4.0 International license (https://creativecommons.org/licenses/by/4.0/) in [30].

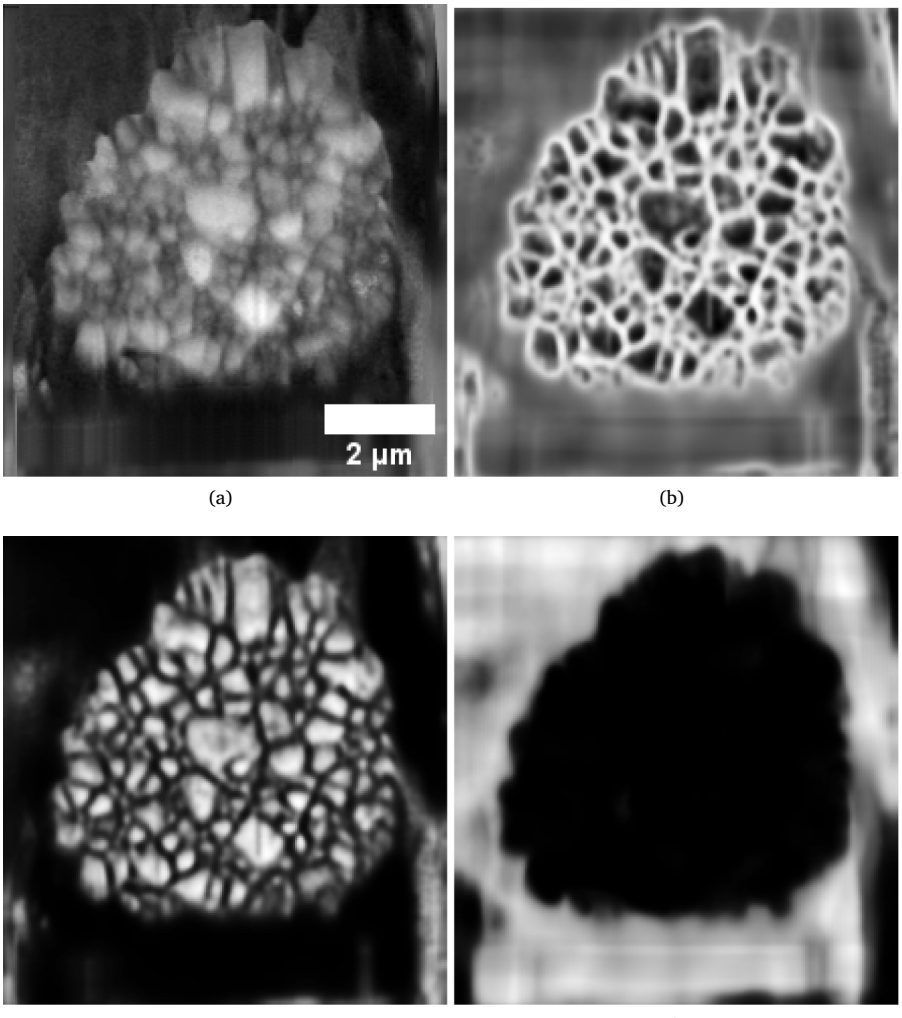

Fig. 4. Visual validation of the neural network. Planar 2D section through the aligned EBSD IQ image I for which no labeling of grain boundaries, grain interiors and background is available (a). The corresponding predictions $\widehat{G}_b$ (b), $\widehat{G}_i$ (c) and $\widehat{B}$ (d) of the trained CNN.

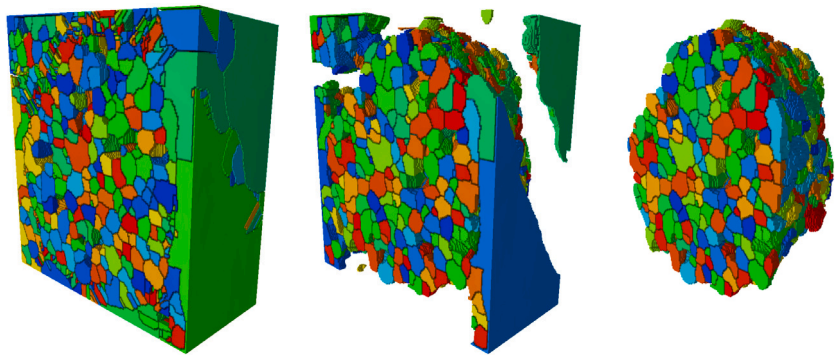

(a) (b) (c)

Fig. 5. Segmentation result (a) of the watershed algorithm applied on the h-minima transformed grain boundary predictions $\widehat{G}_b$. Each region is colored individually. Segmentation (b) after setting the background to 0. Final segmentation result (c) after removing regions outside of the considered NMC particle.

2.4. Computation of grain characteristics

The grain-wise segmentation of the NMC particle achieved in Section 2.3 allows us to compute various characteristics for each individual grain depicted in the segmented image, which we denote by $G_1, \dots, G_n \subset W$ from here on. The considered characteristics efficiently describe the size and shape of grains, i.e., the complex voxelized image data is reduced to vectors of grain characteristics which will then be used for modeling their (multivariate) distributions in Sections 2.5 and 2.6. Now, we describe the characteristics of single grains considered in the present paper, see Fig. 6 for an illustration. In order to reduce so-called edge effects we only compute the characteristics of those grains G which are not cut off by the sampling window W, i.e., $G \subset \{2, \dots, 235-1\} \times \{2, \dots, 221-1\} \times \{2, \dots, 91-1\}$.

The size of a grain G is characterized by its volume-equivalent diameter $d(G)$ given by

$$d(G) = \sqrt[3]{\frac{6V(G)}{\pi}}, \tag{8}$$

where $V(G)$ denotes the volume of G which is estimated by multiplying the number of voxels associated with G with a single voxel's volume.

For analyzing the shape of grains we consider several characteristics. First, for each grain G we compute the sphericity factor $s(G)$ given by

$$s(G) = \frac{\sqrt[3]{36\pi V(G)^2}}{a(G)}, \tag{9}$$

where $a(G)$ denotes the surface area of G which is estimated using the method presented in [37]. Note that the sphericity factor $s(G) \in [0, 1]$ of a grain G describes how close its shape is to that of a perfect sphere, in which case we have $s(G) = 1$.

Another common shape characteristic of G is the convexity $c(G)$ given by

$$c(G) = \frac{V(G)}{V(q(G))}, \tag{10}$$

where $q(G)$ is the discrete convex hull of G on the lattice of W. The convexity measures how much the shape of a grain deviates from convexity. This is of special interest for choosing appropriate stochastic models which can randomly generate virtual but statistically similar grain microstructures as observed in the data. For example, in materials science so-called Voronoi and Laguerre tessellations are widely used for modeling polycrystalline materials [16,38]. However, the microstructures generated by these models solely consist of convex grains. Thus, if primarily non-convex grains are observed in the data, i.e., if typically $c(G) < 1$, these models may not be appropriate.

The elongation $e(G)$ of a grain G is given by the fraction of the smallest and largest half-axes lengths of the best fitting ellipsoid determined by means of principle component analysis (PCA) [39]. In order

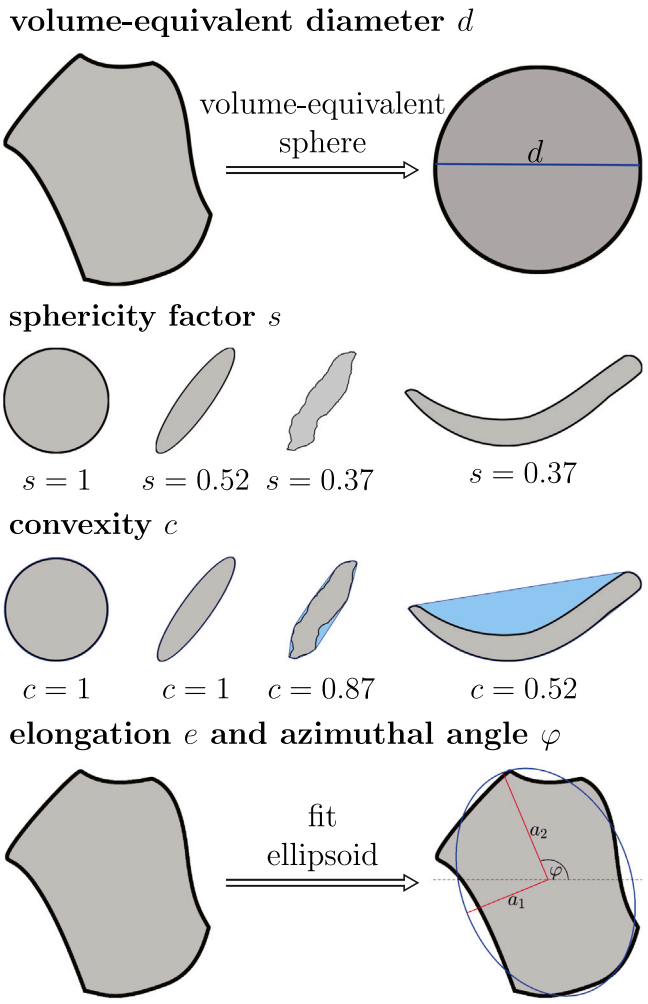

Fig. 6. Illustration of morphological characteristics. For simplicity, the geometrical objects (grains, particles) are depicted in 2D. First row: The volume-equivalent diameter d of an object in 3D is the diameter of a sphere which has the same volume. Second row: The sphericity factor s measures the deviation of the object's shape from a sphere, by comparing the volume and surface of the considered object. Third row: The convexity c is computed by dividing the volume of the object (black) by the volume of its convex hull (blue). Fourth row: For computing the elongation e of an object and the angles describing its main orientation, the best fitting ellipsoid (blue) is determined. The elongation e is the fraction between the smallest and largest half-axes (red) of the ellipsoid. By transforming the vector which points into the direction of the largest half-axis into spherical coordinates the azimuthal angle φ and the polar angle θ (only in 3D) are computed. (For interpretation of the references to color in this figure legend, the reader is referred to the web version of this article.)

to compute the PCA of G we first compute its centroid $\overline{x} = (\overline{x}_1, \overline{x}_2, \overline{x}_3)$ given by

$$\overline{x}_i = \frac{1}{V(G)} \sum_{(x_1,x_2,x_3)\in G} x_i \tag{11}$$

for $i = 1, 2, 3$. Then, we compute the grain's positive definite covariance matrix A, where

$$A = \left(\frac{1}{V(G)} \sum_{(x_1,x_2,x_3)\in G} (x_i - \overline{x}_i)(x_j - \overline{x}_j) \right)_{i,j=1,2,3}. \tag{12}$$

Due to the positive definiteness of A we can compute its eigenvalues $0 \le \lambda_1 \le \lambda_2 \le \lambda_3$ with their corresponding eigenvectors $v_1, v_2, v_3 \in \mathbb{R}^3$. Without loss of generality, we can assume that the third component of these eigenvectors is non-negative, since both v_i and $-v_i$ are eigenvectors of the eigenvalue λ_i. Note that the square roots of the eigenvalues λ_i are proportional to the half axis lengths a_i of the best fitting ellipsoid, i.e., $a_i \propto \sqrt{\lambda_i}$. Thus, the elongation $e(G)$ of G is given by

$$e(G) = \frac{a_1}{a_3} = \sqrt{\frac{\lambda_1}{\lambda_3}}. \tag{13}$$

From the PCA we can also investigate the orientation of single grains. Note that, in this context, the orientation of a grain does not refer to the orientation of its crystallographic lattice. But we call the direction of the eigenvector v_3, i.e., the direction of the largest half-axis of the best fitting ellipsoid, the orientation of the grain. We describe the eigenvector v_3 by its azimuthal angle φ and polar angle θ, i.e.,

$$v_3 = \begin{pmatrix} \sin\theta\cos\varphi \\ \sin\theta\sin\varphi \\ \cos\theta \end{pmatrix}, \tag{14}$$

where $\varphi \in [-\pi, \pi)$ and $\theta \in [0, \pi/2)$. Note that the polar angle θ cannot be larger than $\pi/2$ since the third component of v_3 is non-negative.

2.5. Stochastic modeling of single grain characteristics

We computed the grain characteristics described in Section 2.4 for each individual grain $G_1, \dots, G_n$ which we extracted from EBSD data. Thus, for each grain G_i we determined the vector $(d(G_i), s(G_i), c(G_i), e(G_i))$ of size and shape characteristics and the vector (θ_i, φ_i) of angles describing its orientation. In this section, we shortly explain the procedure for parametrically modeling the probability distributions of these grain characteristics. The stochastic description of (vectors of) microstructure characteristics will serve as reference for fitting parametric models of the entire 3D grain network of NMC particles in a forthcoming study which can be used to generate virtual but realistic 3D inner-particle microstructures.

We start by shortly describing the procedure for modeling the distribution of the volume-equivalent diameter d. For more details, we refer the reader to [13]. The histogram of the values $d(G_1), \dots, d(G_n)$ is depicted in Fig. 7a. By means of maximum likelihood estimation [33] we are able to fit a distribution from various parametric families of probability distributions (e.g., log-normal, gamma, Weibull distribution) to the histogram. Among these parametric fits the best candidate is chosen using the Akaike information criterion which considers the goodness of fit while trying to reduce the number of parameters to avoid overfitting [33]. The resulting fit of the volume-equivalent diameter with the inverse Gaussian distribution is depicted in Fig. 7a (red curve). Analogously, the probability distributions of the sphericity factor s, the convexity c and elongation e are fitted, see Figs. 7b–7d and Table 1.

2.6. Stochastic modeling of pairs of grain characteristics

In the previous section we described the procedure for modeling the distributions of single grain characteristics which, however, provide no information on their correlation structure. For that purpose multivariate probability distributions are more informative since they can describe the entire correlation structure of the considered characteristics. Thus, they are more suited than univariate distributions for fitting and validating stochastic microstructure models of the entire grain architecture which will be considered in a forthcoming study.

For correlated and normally distributed characteristics the multivariate normal distribution provides easy access to modeling the joint distribution of vectors of characteristics. However, as it can be seen in Fig. 7 the grain characteristics considered in the present paper are not normally distributed, yet they are (partially) highly correlated, as seen in Table 3. Therefore, we use so-called copulas to model joint distributions of pairs of grain characteristics [34]. In the following, we shortly describe this modeling approach. For more details we refer the reader to [13].

Let $(x_1, y_1), \dots, (x_n, y_n)$ be n pairs of grain characteristics. Furthermore, let $f_1, f_2 : \mathbb{R} \to [0, \infty)$ be probability densities fitted to the histograms of the first and second characteristic, respectively. Recall that Section 2.5 deals with the parametric modeling of such probability densities. For technical reasons we require the cumulative distribution functions F_i to be absolutely continuous, i.e., to be given by

$$F_i(x) = \int_{-\infty}^{x} f_i(y)\,\mathrm{d}y, \tag{15}$$

for $i = 1, 2$ and all $x \in \mathbb{R}$. Then, using a so-called copula density $c : \mathbb{R}^2 \to [0, \infty)$ we can construct a bivariate probability density $f : \mathbb{R}^2 \to [0, \infty)$ via

$$f(x, y) = f_1(x) f_2(y) c(F_1(x), F_2(y)), \tag{16}$$

the marginal probability densities of which are f_1 and f_2. Simply speaking, a copula density c is a "normalized" bivariate probability density, whose marginal probability densities are the probability density of the uniform distribution on the interval $[0, 1]$. Note that, similar to there being families of univariate probability densities, such as the normal, log-normal, gamma or beta distribution, there are various parametric families of copula densities [40]. Consequently, by considering different parametric copula densities c in Eq. (16) we have various parametric families of bivariate probability densities whose marginal densities coincide with f_1 and f_2. Then, analogously to Section 2.5, bivariate fits from these families of probability distributions can be determined using maximum likelihood estimation and among these fits the best is chosen according to the Akaike information criterion. In the present paper, we considered the following parametric families of copulas: Ali–Mikhail–Haq, Clayton, Frank, Gumbel, Joe, Clayton–Gumbel, Joe–Frank, BB3, BB5 copula [40]. Furthermore, by rotating copulas from a parametric copula family in 90° steps we obtain further parametric families.

3. Results

3.1. Fitted univariate probability densities

In Section 2.5 we described the procedure for fitting univariate probability densities to histograms of grain characteristics. Recall that for the volume-equivalent diameter the inverse Gaussian distribution provided the best fit, the probability density of which is given by

$$f(x) = \begin{cases} \sqrt{\frac{\lambda}{2\pi x^3}} \exp\left(-\frac{\lambda(x-\mu)^2}{2\mu^2 x}\right), & \text{if } x > 0, \\ 0, & \text{else,} \end{cases} \tag{17}$$

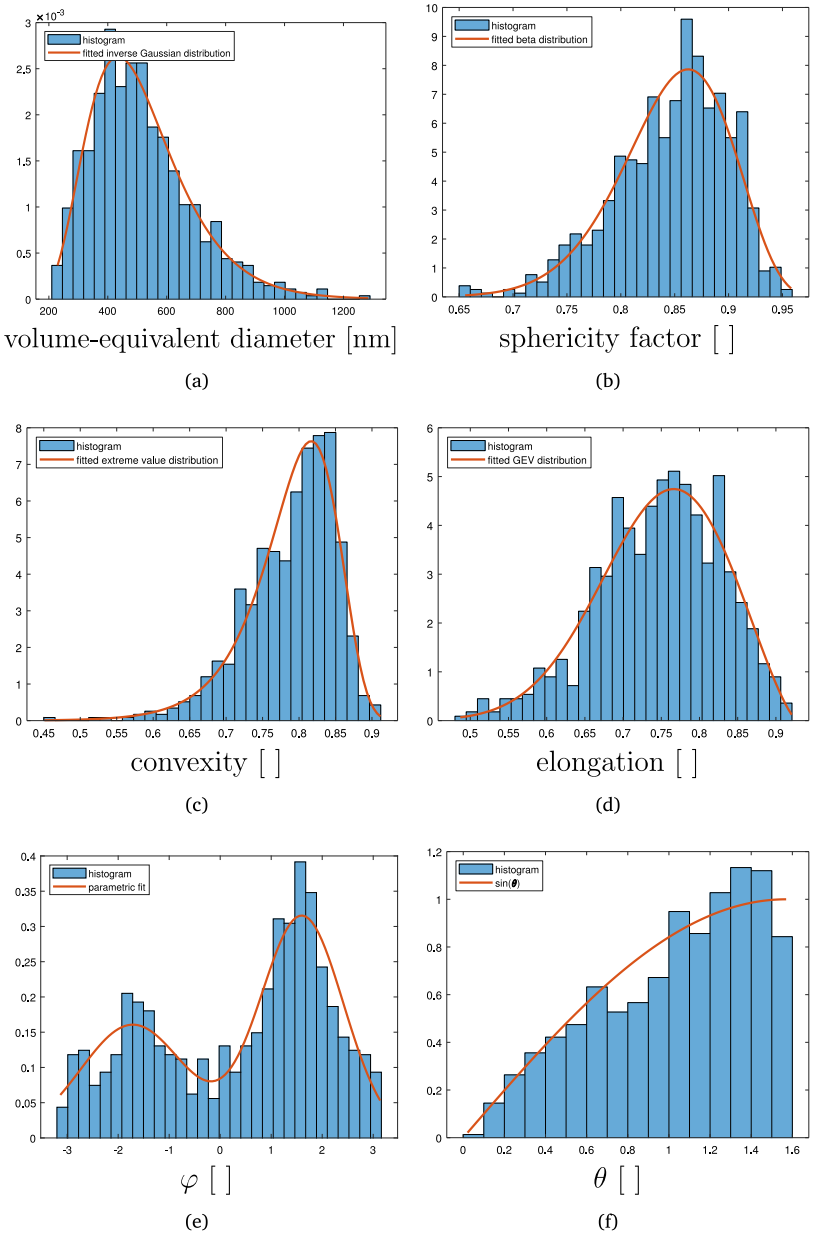

Fig. 7. Histograms (blue) of the volume-equivalent diameter (a), sphericity factor (b), convexity (c), elongation (d) and of the orientation angles (e, f) with bin widths of 36 nm, 0.01, 0.015, 0.014, 0.21, 0.1, respectively. Parametrically fitted probability densities are visualized in red. Note that the probability densities f are normalized, i.e., $\int_{-\infty}^{\infty} f(x)\,\mathrm{d}x = 1$.

where $\mu, \lambda > 0$ are model parameters. Furthermore, we fitted the distribution of the sphericity factor using the beta distribution which has the probability density

$$f(x) = \begin{cases} \frac{1}{B(a,b)} x^{a-1}(1-x)^{b-1}, & \text{if } x \in [0,1], \\ 0, & \text{else}, \end{cases} \tag{18}$$

where $a, b > 0$ are model parameters and B denotes the Beta function. The probability density of the generalized extreme value distribution which was used to fit the distributions of the convexity and the elongation is given by

$$f(x) = \begin{cases} \frac{1}{\sigma} \exp(-(1+k\frac{x-\mu}{\sigma})^{-\frac{1}{k}})(1+k\frac{x-\mu}{\sigma})^{-1-\frac{1}{k}}, & \text{if } k \neq 0 \text{ and } 1+k\frac{x-\mu}{\sigma} > 0 \\ \frac{1}{\sigma} \exp\left(-\exp(-\frac{x-\mu}{\sigma}) - \frac{x-\mu}{\sigma}\right), & \text{if } k = 0, \\ 0, & \text{else}, \end{cases} \tag{19}$$

where $k, \mu \in \mathbb{R}$ and $\sigma > 0$ are model parameters. The parametric fits for the probability densities of d, s, c, e are depicted in Figs. 7a–7d. Their corresponding parameters are listed in Table 1.

For modeling the distribution of the azimuthal orientation angle φ we chose a special parametric family of distributions. More precisely, the shape of the histogram of the angles $\varphi_1, \ldots, \varphi_n$ indicates that a bimodal probability density might provide a good fit, see Fig. 7e. Furthermore, due to the fact that the angles belong to the interval $[-\pi, \pi)$, the support of the fitted density should be equal to or a subset of $[-\pi, \pi)$. Therefore, we chose a mixture of two normal distributions truncated on the interval $[-\pi, \pi)$ as a parametric family of distributions whose probability density is given by the proportionality

$$f(\varphi) \propto \begin{cases} \lambda f_{(\mu_1,\sigma_1^2)}(\varphi) + (1-\lambda) f_{(\mu_2,\sigma_2^2)}(\varphi), & \text{if } \varphi \in [-\pi, \pi), \\ 0, & \text{else}, \end{cases} \tag{20}$$

where $\lambda \in [0,1]$ and $f_{(\mu_1,\sigma_1^2)}, f_{(\mu_2,\sigma_2^2)}$ are the probability densities of normal distributions with mean values μ_1, μ_2 and variances σ_1^2, σ_2^2,

Table 1
Parameters of fitted univariate probability densities depicted in Fig. 7. Formulas for the probability densities of the parametric families of distributions are given in Eqs. (17), (18), (19), (20) and (21).

Characteristic	Family of distributions	Parameter values
Volume-equivalent diameter d	Inverse Gaussian	$\mu = 513.8,\ \lambda = 4600$
Sphericity factor s	Beta	$a = 40.1,\ b = 7.2$
Convexity c	Generalized extreme value[a]	$k = 0,\ \mu = 0.82,\ \sigma = 0.048$
Elongation e	Generalized extreme value[a]	$k = -0.42,\ \mu = 0.72,\ \sigma = 0.086$
Azimuthal angle φ	Gaussian mixture according to (20)	$\mu_1 = -1.7,\ \mu_2 = 1.6,\ \sigma_1 = 1,\ \sigma_2 = 0.8,\ \lambda = 0.4$
Polar angle θ	$\sin(\cdot)$	–

[a]Distribution was truncated on the interval $[0, 1]$.

Table 2
Comparison of aggregated quantities (mean values, standard deviations) computed for samples of grain characteristics extracted from tomographic image data, and for the fitted parametric probability densities, respectively.

Characteristic	Empirical mean value	Mean value fitted of the distribution	Empirical std	Std of the fitted distribution
Volume-equivalent diameter d	513.81	513.81	172.56	171.99
Sphericity factor s	0.85	0.85	0.053	0.052
Convexity c	0.79	0.79	0.062	0.062
Elongation e	0.75	0.75	0.081	0.081
Azimuthal angle φ	0.39	0.43	1.70	1.30
Polar angle θ	1.03	1	0.382	0.376

Table 3
Correlation coefficients for pairs of the considered grain characteristics computed for samples of grain characteristics extracted from tomographic image data, and for the fitted bivariate probability densities, respectively.

Pairs of characteristics	Empirical correlation coefficient	Correlation coefficient of the parametric fit
(d, s)	−0.4680	−0.4612
(d, c)	−0.3418	−0.3632
(s, c)	0.9209	0.9115
(s, e)	0.6757	0.6570
(c, e)	0.5100	0.4827
(θ, φ)	−0.0473	−0.0525

Table 4
Copula parameters of the bivariate probability densities depicted in Fig. 8. Formulas for the copula densities of the parametric families of copulas are given in Eqs. (22) and (23).

Pairs of characteristics	Copula family	Parameter values	Copula rotation
(d, s)	Joe–Frank	$\kappa = 4.24, \delta = 0.6$	270°
(d, c)	Joe–Frank	$\kappa = 2.7, \delta = 0.7$	270°
(s, c)	Clayton–Gumbel	$\kappa = 0.36, \delta = 3.13$	180°
(s, e)	Clayton–Gumbel	$\kappa = 0.47, \delta = 1.47$	0°
(c, e)	Joe–Frank	$\kappa = 5.6, \delta = 0.52$	180°
(θ, φ)	Joe–Frank	$\kappa = 1.1, \delta = 0.82$	270°

respectively. Then, we determined an optimal fit from this model with five parameters using a maximum likelihood approach, see Fig. 7f and Table 1.

Finally, note that in the case of the orientation vectors v_3 being uniformly distributed on the upper hemi-sphere their polar angle's distribution has the probability density

$$f(\theta) = \begin{cases} \sin(\theta), & \text{if } \theta \in [0, \pi/2), \\ 0, & \text{else.} \end{cases} \tag{21}$$

Fig. 7f indicates that the probability density given in (21) fits the histogram of the angles $\theta_1, \ldots, \theta_n$ computed from the image data quite well.

Looking at Fig. 7 we get an impression of the goodness of fit by visual inspection. A more quantitative analysis of the goodness of fit is given in Table 2, where we compare empirical mean values and empirical standard deviations computed for samples of grain characteristics extracted from tomographic image data, with the mean values and standard deviations (std) of the fitted parametric probability densities.

3.2. Fitted bivariate probability densities

In Section 2.6 the procedure for modeling bivariate probability distributions of two-dimensional vectors of grain characteristics using copulas has been described. For pairs of the grain characteristics d, s, c, e which have an empirical correlation coefficient with an absolute value larger than 0.1 (see Table 3) we have applied this method to fit the corresponding bivariate probability densities, which are visualized in Fig. 8a–f.

The family of parametric copulas which provided the best fit and their corresponding parameters are listed in Table 4. Note that the copula density c of the parametric family of Joe–Frank copulas, which was used for fitting the bivariate distribution of the volume-equivalent diameter and the sphericity factor, is given by

$$c(u, v) = \frac{\partial^2}{\partial u \partial v} \frac{1}{\kappa} \left(1 - \left[1 - \frac{1}{1 - (1 - \delta)^\kappa} (1 - (1 - \delta u)^\kappa)(1 - \delta v)^\kappa \right]^{\frac{1}{\delta}} \right) \tag{22}$$

for each $u, v \in [0, 1]$ with model parameters $\kappa \geq 1$ and $\delta \in (0, 1]$. For fitting the bivariate distribution of the sphericity factor and convexity we used a Clayton–Gumbel copula, the copula density of which is given by

$$c(u, v) = \left(\left((u^{-\kappa} - 1)^\delta + (v^{-\kappa} - 1)^\delta \right)^{1/\delta} + 1 \right)^{-1/\kappa} \tag{23}$$

for each $u, v \in [0, 1]$, where $\kappa > 0$ and $\delta > 1$ are model parameters.

Furthermore, we used the method for fitting bivariate probability densities described above to fit the bivariate probability density of the orientation angles of grains, see Fig. 8f and Table 4. Recall that in Table 2 we quantitatively compared quantities (mean value, std) computed empirically from data and derived from the fitted univariate probability densities. Similarly, we validate the fitted bivariate probability densities by comparing their correlation coefficient with the empirically computed correlation coefficient, see Table 3. Note that the correlation coefficient ρ of a bivariate probability density f is given by

$$\rho = \frac{1}{\sigma_1 \sigma_2} \int_{-\infty}^{\infty} \int_{-\infty}^{\infty} (xy - \mu_1 \mu_2) f(x, y) \, \mathrm{d}x \mathrm{d}y, \tag{24}$$

where μ_1, μ_2 denote the mean values and σ_1, σ_2 the stds of the marginals.

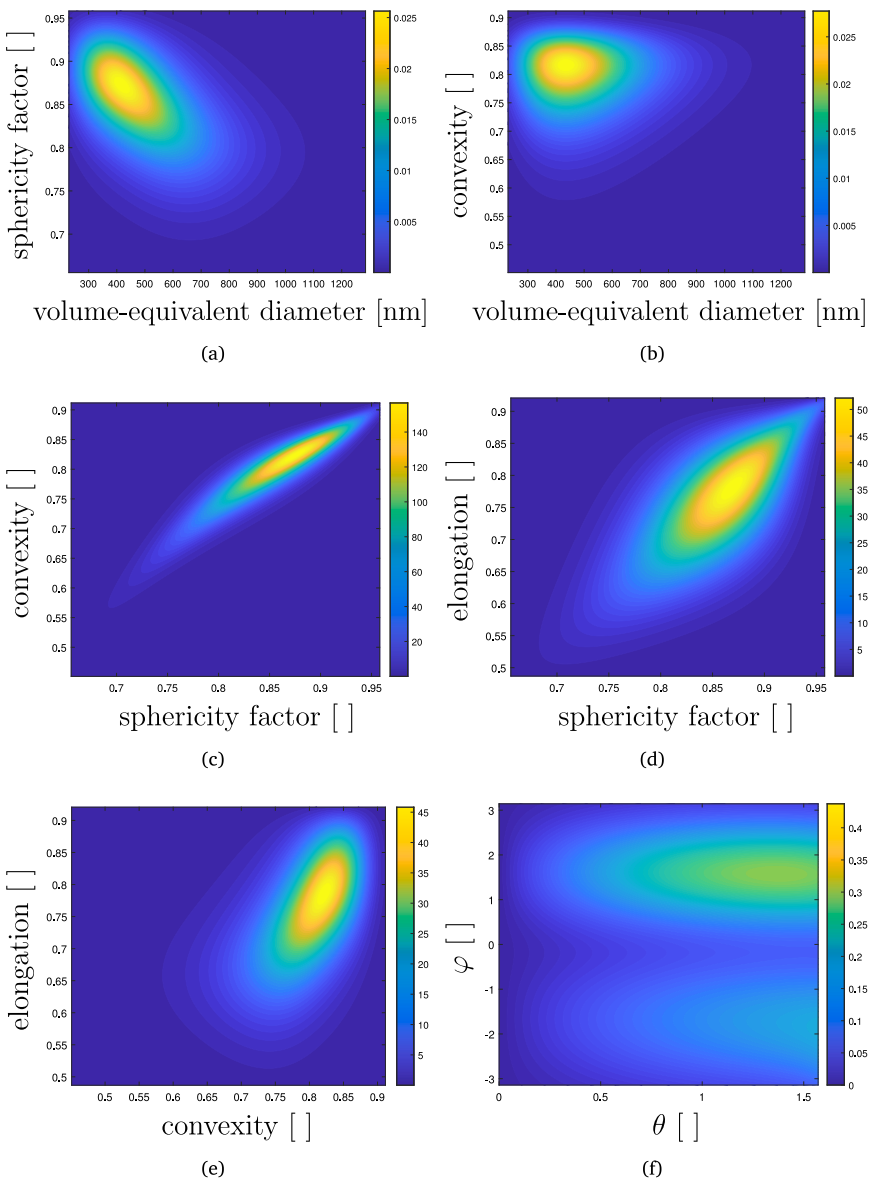

Fig. 8. Bivariate probability densities of the pairs $(d,s),(d,c),(s,c),(s,e),(c,e),(\theta,\varphi)$ (a–f, respectively) of grain characteristics fitted using parametric copulas. Note that bivariate probability densities f are normalized, i.e., $\int_{-\infty}^{\infty}\int_{-\infty}^{\infty} f(x,y)\,\mathrm{d}y\mathrm{d}x = 1$.

3.3. Specific surface area of the grain boundary network

Recall that in Tables 2 and 3 we investigated aggregated quantities computed for samples of (univariate and bivariate) grain characteristics extracted from tomographic image data. Similarly, in the present section we estimate the specific surface area of the entire grain boundary network within a NMC particle which is another kind of an aggregated quantity. Therefore, for each pair (G_i, G_j) of grains in the segmented image data we compute the quantity

$$a_{G_i,G_j} = \frac{1}{2}\left(a(G_i) + a(G_j) - a(G_i \cup G_j)\right), \tag{25}$$

which can be considered as an estimate of the surface area of the shared interface between G_i and G_j.

By summing up the surface areas a_{G_i,G_j} for all pairs G_i, G_j of grains we determine the surface area of the grain boundary network in the sampling window W to be $491.5\,\mu\mathrm{m}^2$. Dividing this quantity by the volume of the observed part of the particle in the sampling window W we obtain the specific surface area of $4.98\,\mu\mathrm{m}^{-1}$.

4. Discussion

The 3D reconstruction and segmentation of grains within an NMC particle facilitated quantification of the microstructural features of sub-particle grains. Grain properties, including the distribution of their volume-equivalent diameters, as well as morphological descriptors like their sphericity, convexity, and elongation, were quantified. Until now, much focus has been on quantifying particle size distributions via X-ray CT [41] which empowers researchers and manufactures to quantify particle size distributions for quality control, for example by determining how narrow a particle size distribution they can achieve for a batch of electrode. Here, we demonstrate how the distributions of sub-particle grain properties can be quantified. The distributions of volume-equivalent diameters and sphericity factors show that most grains are around 400 nm in diameter and have a sphericity factor of about 0.85. These properties are likely to influence the rate capability and propensity of the particle to crack as grains expand and propagate mechanical stress throughout the particle during lithiation. Synthesis

methods could be tuned to selectively change the size, shape, and orientation of grains for higher rate and reduced degradation, for example by designing more radially oriented grains [42]. With the benchmark characterized particle presented here, this architecture could be used for multiphysics modeling, elucidating strain and lithiation heterogeneities during operation. The characterization using multivariate probability densities, see Fig. 8, has the advantage of capturing the correlation structure between the considered grain characteristics. Moreover, it is possible to derive even further distributions of grain characteristics from these multivariate fits if the characteristic under consideration is in a deterministic functional relationship with the grain characteristics for which the multivariate distribution is given. For example, the specific surface area of grains can be directly computed from the volume-equivalent diameter d and the sphericity factor s—thus, the probability density of the specific surface area can be computed from their bivariate probability density depicted in Fig. 8a. Furthermore, the probability densities presented in Figs. 7 and 8 could be used to artificially generate particles with realistic architectures; in a forthcoming study, we will use a parametric stochastic model for the entire 3D grain microstructure of NMC particles based on random tessellations to generate virtual grain architectures. First, we will determine parameter constellations for the stochastic microstructure model for which the distributions of the considered grain characteristics reassemble the distributions derived from the experimental image data considered in the present paper. Then, by systematical variation of the model parameters, we will generate a broad spectrum of different virtual microstructures which will serve as input for numerical simulations, allowing us to correlate geometry descriptors of the microstructure with its macroscopic properties [20–24]. This is expected to enable fast analysis of different single particle architectures and provide a roadmap for synthesizing optimal architectures for specific operating conditions.

Furthermore, the characteristics considered in the present paper for describing NMC particles could be extended to describe even further aspects of their architecture. More precisely, in this work, the uncycled NMC532 particles consisted of solid structures without any signs of sub-particle voids or evidence of cracks. However, cathode particles come in a variety of designs including some with hollow cores [41] and sub-particle voids between grains [6]. Furthermore, NMC particles are known to crack along grain boundaries upon being exposed to certain cycling conditions [3] creating further sub-particle features that are important to segment and distinctly label. Distinctly labeling sub-particle features like cracks and estimating the additional surface area of the cathode that becomes exposed to the electrolyte was recently achieved in [43] for X-ray CT images. This technique of identifying and labeling sub-particle features, like cracks and voids, could also be applied to this data to facilitate linking added exposed surface area upon mechanical degradation of the particles.

5. Conclusion

A fast method to conduct FIB–EBSD of single Li-ion electrode particles for achieving a full 3D reconstruction of particle grain architectures is presented. The experimental technique of FIB–EBSD can be applied to cathode particles with layered structures including all types of NMC materials irrespective of stoichiometry and morphology of grains. The main challenge that may arise is if the particle of interest has grain sizes that are close to the effective resolution of the FIB–EBSD imaging technique, in which case it may not be possible to accurately segment grain boundaries and distinctly label grains. However, if the grain sizes are suitable for the resolution of the used imaging technique, the methodology for processing and quantifying features from the data can be applied. In the present paper, the image quality map from EBSD gave excellent contrast of grain boundaries throughout consecutive FIB slices of an NMC532 particle. Between EBSD imaging and FIB slicing, the sample stage was rotated and tilted and sometimes did not perfectly re-center, necessitating postprocessing image realignment. Following image alignment, machine learning segmentation facilitated identification and labeling of distinct grains in 3D within the particle. The 3D segmented image was used for quantification of sub-particle grain architectures. For example, the grain size distribution within a single particle was quantified, as well as the distributions of morphological descriptors like sphericity, convexity, elongation, and orientations. In this case, the grains were found to be close to spherical and have a distribution of volume-equivalent diameters with a mean around 400 nm, but as observed from other works in literature, these grain properties are expected to vary between differently synthesized electrode blends. This technique is expected to equip researchers with a tool to quantify the sub-particle architectures of their synthesized electrode blends, provided that the electrode particles are crystalline. There is substantial scope for building on this work to understand through further advanced microstructural characterization and image-based multiscale modeling. Future work will utilize the derived bivariate probability densities of pairs of grain characteristics for fitting and validating parametric stochastic geometry models for the holistic 3D grain architecture of NMC particles. In particular, these models will be used to generate random grain architectures for which the bivariate probability densities of pairs of grain characteristics will be computed analogously, and fitted/compared to the bivariate probability densities reported in the present paper. Then, a broad spectrum of statistically different grain architectures, i.e., with different specifications for the distribution of vectors of grain characteristics, will be generated. Even though it might not always be possible to synthesize NMC particles with statistically similar grain architectures as the virtual ones, they still allow for a systematic quantitative investigation of structure–property relationships.

CRediT authorship contribution statement

Orkun Furat: Network training, Segmentation, Analysis of image data, Written main parts of the paper, Discussed the results, Writing of the manuscript. **Donal P. Finegan:** Written main parts of the paper, Discussed the results, Writing of the manuscript. **David Diercks:** Performed FIB–EBSD measurements, Discussed the results, Writing of the manuscript. **Francois Usseglio-Viretta:** Written main parts of the paper, Discussed the results, Writing of the manuscript. **Kandler Smith:** Discussed the results, Writing of the manuscript, Designed and supervised the research. **Volker Schmidt:** Discussed the results, Writing of the manuscript, Designed and supervised the research.

Declaration of competing interest

The authors declare that they have no known competing financial interests or personal relationships that could have appeared to influence the work reported in this paper.

Acknowledgments

This work was authored in part by the National Renewable Energy Laboratory, operated by Alliance for Sustainable Energy, LLC, for the U.S. Department of Energy (DOE) under Contract No. DE-AC36-08GO28308. Funding was provided by the U.S. DOE Office of Vehicle Technology Extreme Fast Charge Program, program manager Samuel Gillard. The views expressed in the article do not necessarily represent the views of the DOE or the U.S. Government. The U.S. Government retains and the publisher, by accepting the article for publication, acknowledges that the U.S. Government retains a nonexclusive, paid-up, irrevocable, worldwide license to publish or reproduce the published form of this work, or allow others to do so, for U.S. Government purposes. Furthermore, this work has been partially supported by the German Research Foundation (DFG) through funding the research project SCHM 997/27-1 within the priority program SPP 2045.

References

[1] Z. Xu, Z. Jiang, C. Kuai, R. Xu, C. Qin, Y. Zhang, M.M. Rahman, C. Wei, D. Nordlund, C.-J. Sun, et al., Charge distribution guided by grain crystallographic orientations in polycrystalline battery materials, Nature Commun. 11 (1) (2020) 1–9, http://dx.doi.org/10.1038/s41467-019-13884-x.

[2] A. Mukhopadhyay, B.W. Sheldon, Deformation and stress in electrode materials for Li-ion batteries, Prog. Mater. Sci. 63 (2014) 58–116, http://dx.doi.org/10.1016/j.pmatsci.2014.02.001.

[3] P. Yan, J. Zheng, M. Gu, J. Xiao, J.-G. Zhang, C.-M. Wang, Intragranular cracking as a critical barrier for high-voltage usage of layer-structured cathode for lithium-ion batteries, Nature Commun. 8 (1) (2017) 1–9, http://dx.doi.org/10.1038/ncomms14101.

[4] H. Liu, M. Wolf, K. Karki, Y.-S. Yu, E.A. Stach, J. Cabana, K.W. Chapman, P.J. Chupas, Intergranular cracking as a major cause of long-term capacity fading of layered cathodes, Nano Lett. 17 (6) (2017) 3452–3457, http://dx.doi.org/10.1021/acs.nanolett.7b00379.

[5] S.-H. Lee, C. Yoon, K. Amine, Y.-K. Sun, Improvement of long-term cycling performance of $Li[Ni_{0.8}Co_{0.15}Al_{0.05}]O_2$ by AlF_3 coating, J. Power Sources 234 (2013) 201–207, http://dx.doi.org/10.1016/j.jpowsour.2013.01.045.

[6] D.P. Finegan, A. Vamvakeros, C. Tan, T.M. Heenan, S.R. Daemi, N. Seitzman, M. Di Michiel, S. Jacques, A.M. Beale, D.J. Brett, et al., Spatial quantification of dynamic inter and intra particle crystallographic heterogeneities within lithium ion electrodes, Nature Commun. 11 (1) (2020) 1–11, http://dx.doi.org/10.1038/s41467-020-14467-x.

[7] F. Humphreys, Review grain and subgrain characterisation by electron backscatter diffraction, J. Mater. Sci. 36 (16) (2001) 3833–3854, http://dx.doi.org/10.1023/A:1017973432592.

[8] S.I. Wright, M.M. Nowell, BESD image quality mapping, Microsc. Microanal. 12 (1) (2006) 72, http://dx.doi.org/10.1017/S1431927606060090.

[9] A. Quinn, H. Moutinho, F. Usseglio-Viretta, A. Verma, K. Smith, M. Keyser, D.P. Finegan, Electron backscatter diffraction for investigating lithium-ion electrode particle architectures, Cell Rep. Phys. Sci. 1 (8) (2020) 100137, http://dx.doi.org/10.1016/j.xcrp.2020.100137.

[10] M. Groeber, B. Haley, M. Uchic, S. Ghosh, Microstructural characterization using 3-d orientation data collected by an automated FIB-EBSD system, in: S. Ghosh, J.K. Lee, J.C. Castro (Eds.), AIP Conference Proceedings, 712, American Institute of Physics, 2004, pp. 1712–1718, http://dx.doi.org/10.1063/1.1766778.

[11] M. Neumann, J. Staněk, O.M. Pecho, L. Holzer, V. Beneš, V. Schmidt, Stochastic 3D modeling of complex three-phase microstructures in SOFC-electrodes with completely connected phases, Comput. Mater. Sci. 118 (2016) 353–364, http://dx.doi.org/10.1016/j.commatsci.2016.03.013.

[12] O. Furat, T. Leißner, R. Ditscherlein, O. Šedivý, M. Weber, K. Bachmann, J. Gutzmer, U. Peuker, V. Schmidt, Description of ore particles from X-Ray microtomography (XMT) images, supported by scanning electron microscope (SEM)-based image analysis, Microsc. Microanal. 24 (5) (2018) 461–470, http://dx.doi.org/10.1017/S1431927618015076.

[13] O. Furat, T. Leißner, K. Bachmann, J. Gutzmer, U. Peuker, V. Schmidt, Stochastic modeling of multidimensional particle properties using parametric copulas, Microsc. Microanal. 25 (3) (2019) 720–734, http://dx.doi.org/10.1017/S1431927619000321.

[14] J. Kopeček, J. Staněk, S. Habr, F. Seitl, L. Petrich, V. Schmidt, V. Beneš, Analysis of polycrystalline microstructure of AlMgSc alloy observed by 3D EBSD, Image Anal. Stereol. 39 (1) (2020) 1–11, http://dx.doi.org/10.5566/ias.2224.

[15] K. Kuchler, B. Prifling, D. Schmidt, H. Markoetter, I. Manke, T. Bernthaler, V. Knoblauch, V. Schmidt, Analysis of the 3D microstructure of experimental cathode films for lithium-ion batteries under increasing compaction, J. Microsc. 272 (2) (2018) 96–110, http://dx.doi.org/10.1111/jmi.12749.

[16] A. Okabe, B. Boots, K. Sugihara, S.N. Chiu, Spatial Tessellations: Concepts and Applications of Voronoi Diagrams, J. Wiley & Sons, 2009.

[17] S.N. Chiu, D. Stoyan, W.S. Kendall, J. Mecke, Stochastic Geometry and its Applications, J. Wiley & Sons, 2013.

[18] M. Chouchane, A. Rucci, T. Lombardo, A.C. Ngandjong, A.A. Franco, Lithium ion battery electrodes predicted from manufacturing simulations: Assessing the impact of the carbon-binder spatial location on the electrochemical performance, J. Power Sources 444 (2019) 227285, http://dx.doi.org/10.1016/j.jpowsour.2019.227285.

[19] D. Zhang, A. Bertei, F. Tariq, N. Brandon, Q. Cai, Progress in 3D electrode microstructure modelling for fuel cells and batteries: transport and electrochemical performance, Prog. Energy 1 (1) (2019) 012003, http://dx.doi.org/10.1088/2516-1083/ab38c7.

[20] S. Barman, H. Rootzén, D. Bolin, Prediction of diffusive transport through polymer films from characteristics of the pore geometry, AIChE J. 65 (1) (2019) 446–457, http://dx.doi.org/10.1002/aic.16391.

[21] H. Moussaoui, R.K. Sharma, J. Debayle, Y. Gavet, G. Delette, J. Laurencin, Microstructural correlations for specific surface area and triple phase boundary length for composite electrodes of solid oxide cells, J. Power Sources 412 (2019) 736–748, http://dx.doi.org/10.1016/j.jpowsour.2018.11.095.

[22] M. Neumann, O. Furat, D. Hlushkou, U. Tallarek, L. Holzer, V. Schmidt, On microstructure-property relationships derived by virtual materials testing with an emphasis on effective conductivity, in: M. Baum, G. Brenner, J. Grabowski, T. Hanschke, S. Hartmann, A. Schöbel (Eds.), Simulation Science, Springer, 2017, pp. 145–158, http://dx.doi.org/10.1007/978-3-319-96271-9_9.

[23] M. Neumann, O. Stenzel, F. Willot, L. Holzer, V. Schmidt, Quantifying the influence of microstructure on effective conductivity and permeability: virtual materials testing, Int. J. Solids Struct. 184 (2020) 211–220, http://dx.doi.org/10.1016/j.ijsolstr.2019.03.028.

[24] F.L.E. Usseglio-Viretta, D.P. Finegan, A. Colclasure, T.M.M. Heenan, D. Abraham, P. Shearing, K. Smith, Quantitative relationships between pore tortuosity, pore topology, and solid particle morphology using a novel discrete particle size algorithm, J. Electrochem. Soc. 167 (10) (2020) 100513, http://dx.doi.org/10.1149/1945-7111/ab913b.

[25] I. Goodfellow, Y. Bengio, A. Courville, Deep learning, MIT Press, 2016.

[26] W. Burger, M.J. Burge, Digital Image Processing: An Algorithmic Introduction Using Java, Springer, 2016.

[27] X. Zhenying, Z. Jiandong, Z. Qi, P. Yamba, Algorithm based on regional separation for automatic grain boundary extraction using improved mean shift method, Surf. Topogr.: Metrol. Prop. 6 (2) (2018) 025001, http://dx.doi.org/10.1088/2051-672x/aab73b.

[28] A. Spettl, R. Wimmer, T. Werz, M. Heinze, S. Odenbach, C. Krill III, V. Schmidt, Stochastic 3D modeling of ostwald ripening at ultra-high volume fractions of the coarsening phase, Modelling Simulation Mater. Sci. Eng. 23 (6) (2015) 065001, http://dx.doi.org/10.1088/0965-0393/23/6/065001.

[29] O. Ronneberger, P. Fischer, T. Brox, U-net: Convolutional networks for biomedical image segmentation, Comput. Res. Repos. (2015) arXiv:1505.04597.

[30] O. Furat, M. Wang, M. Neumann, L. Petrich, M. Weber, C.E. Krill III, V. Schmidt, Machine learning techniques for the segmentation of tomographic image data of functional materials, Front. Mater. 6 (2019) 145, http://dx.doi.org/10.3389/fmats.2019.00145.

[31] Ö. Çiçek, A. Abdulkadir, S.S. Lienkamp, T. Brox, O. Ronneberger, 3d U-net: Learning dense volumetric segmentation from sparse annotation, Computing Research Repository (2016) arXiv:1606.06650.

[32] P. Soille, Morphological Image Analysis: Principles and Applications, Springer, 2013.

[33] L. Held, D.S. Bové, Applied Statistical Inference, Springer, 2014.

[34] R.B. Nelsen, An Introduction to Copulas, Springer, 2007.

[35] P. Thevenaz, U.E. Ruttimann, M. Unser, A pyramid approach to subpixel registration based on intensity, IEEE Trans. Image Process. 7 (1) (1998) 27–41, http://dx.doi.org/10.1109/83.650848.

[36] D.P. Kingma, J. Ba, Adam: A method for stochastic optimization, Comput. Res. Repos. (2014) arXiv:1412.6980.

[37] K. Schladitz, J. Ohser, W. Nagel, Measuring intrinsic volumes in digital 3D images, in: A. Kuba, L.G. Nyúl, K. Palágyi (Eds.), International Conference on Discrete Geometry for Computer Imagery, Springer, 2006, pp. 247–258, http://dx.doi.org/10.1007/11907350_21.

[38] O. Šedivỳ, D. Westhoff, J. Kopeček, C.E. Krill III, V. Schmidt, Data-driven selection of tessellation models describing polycrystalline microstructures, J. Stat. Phys. 172 (5) (2018) 1223–1246, http://dx.doi.org/10.1007/s10955-018-2096-8.

[39] T. Hastie, R. Tibshirani, J. Friedman, The Elements of Statistical Learning: Data Mining, Inference, and Prediction, Springer, 2009.

[40] H. Joe, Dependence Modeling with Copulas, CRC Press, 2014.

[41] T.M. Heenan, A.V. Llewellyn, A.S. Leach, M.D. Kok, C. Tan, R. Jervis, D.J. Brett, P.R. Shearing, Resolving li-ion battery electrode particles using rapid lab-based X-Ray nano-computed tomography for high-throughput quantification, Adv. Sci. (2020) 2000362, http://dx.doi.org/10.1002/advs.202000362.

[42] J.-G. Wang, F. Li, H.-J. Zhou, P.-C. Sun, D.-T. Ding, T.-H. Chen, Silica hollow spheres with ordered and radially oriented amino-functionalized mesochannels, Chem. Mater. 21 (4) (2009) 612–620, http://dx.doi.org/10.1002/aenm.201803963.

[43] L. Petrich, D. Westhoff, J. Feinauer, D.P. Finegan, S.R. Daemi, P.R. Shearing, V. Schmidt, Crack detection in lithium-ion cells using machine learning, Comput. Mater. Sci. 136 (2017) 297–305, http://dx.doi.org/10.1016/j.commatsci.2017.05.012.